INTERNATIONAL JOURNAL FOR NUMERICAL METHODS IN FLUIDS
Int. J. Numer. Meth. Fluids (2012)
Published online in Wiley Online Library (wileyonlinelibrary.com/journal/nmf). DOI: 10.1002/fld.3743

Numerical prediction of turbulent flows using Reynolds-averaged Navier–Stokes and large-eddy simulation with uncertain inflow conditions

Pietro Marco Congedo[1,*,†], Cedric Duprat[2], Guillaume Balarac[2] and Christophe Corre[2]

[1] *BACCHUS Team, INRIA Bordeaux Sud-Ouest, 351 Cours de la Libération, 33405 Talence Cedex, France*
[2] *Grenoble-INP/UJF Grenoble 1/CNRS, LEGI UMR 5519 Domaine Universitaire BP 53, 38041 Grenoble Cedex 9, France*

SUMMARY

Numerous comparisons between Reynolds-averaged Navier–Stokes (RANS) and large-eddy simulation (LES) modeling have already been performed for a large variety of turbulent flows in the context of fully deterministic flows, that is, with fixed flow and model parameters. More recently, RANS and LES have been separately assessed in conjunction with stochastic flow and/or model parameters. The present paper performs a comparison of the RANS $k - \epsilon$ model and the LES dynamic Smagorinsky model for turbulent flow in a pipe geometry subject to uncertain inflow conditions. The influence of the experimental uncertainties on the computed flow is analyzed using a non-intrusive polynomial chaos approach for two flow configurations (with or without swirl). Measured quantities including an estimation of the measurement error are then compared with the statistical representation (mean value and variance) of their RANS and LES numerical approximations in order to check whether experiment/simulation discrepancies can be explained within the uncertainty inherent to the studied configuration. The statistics of the RANS prediction are found in poor agreement with experimental results when the flow is characterized by a strong swirl, whereas the computationally more expensive LES prediction remains statistically well inside the measurement intervals for the key flow quantities.

Received 1 August 2011; Revised 18 September 2012; Accepted 23 September 2012

KEY WORDS: uncertainties quantification; turbulence modeling

1. INTRODUCTION

The pros and cons of Reynolds-averaged Navier–Stokes (RANS) simulations and large-eddy simulations (LES) are now well established in the context of fully deterministic flows, that is, when the physical flow conditions on one hand and the numerical parameters on the other hand (such as the turbulence or subgrid-scale model parameters) are all assumed to be exactly known. Comparative assessments of RANS/LES modeling can be found not only in the classical context of aerodynamic studies [1–3], combustion [4], meteorology [5], and architectural fluid mechanics [6, 7] but also for less standard applications dealing for instance with accurate rain measurements [8], electronic system cooling design [9], sediment transport [10], or chemical and process engineering [11].

Deterministic comparisons between turbulent flow solvers are now identified as insufficient to provide a valid assessment of their respective predictive potential. A first reason to believe that a purely deterministic comparison is flawed comes from the process followed to obtain the reference experimental data usually used to assess the superior accuracy of one model with respect to the other. Because the available measured data for a flow experiment are usually averaged quantities over a set

*Correspondence to: Pietro Marco Congedo, BACCHUS Team, INRIA Bordeaux Sud-Ouest, 351 Cours de la Libération, 33405 Talence Cedex, France.
†E-mail: pietro.congedo@inria.fr

of experimental realizations, it seems indeed advisable to compare these statistical measurements with similarly measured numerical quantities, that is, computed with a probabilistic description of the operating conditions rather than a deterministic one. This type of observation may also lead to reconsideration of the whole derivation process of turbulence models and more generally closure models (thermodynamic equations of state for instance) as model calibration should be performed on the basis of a statistical description for both experiments and computations [12, 13]. Stochastic computational mechanics is a very active emerging field providing the necessary tools that have to be coupled with existing computational fluid dynamics (CFD) solvers in order to quantify the impact of uncertainty on numerical results [14, 15]. When restricting the review of the uncertainty quantification (UQ) and CFD literature to the assessment of turbulent flow solvers, only few works can be found. Lucor *et al*. [16] have used polynomial chaos to study the sensitivity of LES to subgrid-scale-model parametric uncertainty. Ko *et al*. [17] have examined the sensitivity of direct numerical simulations (DNS) of two-dimensional spatially developing plane mixing layers to uncertainties in the inflow boundary conditions, applying a stochastic collocation method based on the generalized polynomial chaos. Recently, Han *et al*. [18] have performed a similar analysis, applying again generalized polynomial chaos to account for uncertain inflow conditions, in the case of the massively separated flow around a square cylinder computed with a well-established two-equation RANS model. A few other works such as [19–21] deal with UQ and the analysis of turbulent flows, but to the best of our knowledge no contribution has yet dealt with a comparative assessment of RANS and LES modeling on the same flow configuration when taking into account the uncertainties associated with this configuration.

The original objective of the present work is therefore twofold: (i) to estimate on the same industrial flow the predictive quality of LES and RANS approaches when uncertainties are included in the numerical prediction; (ii) to quantify the effects of the physical uncertainties both on RANS and LES modeling. The method used to take into account uncertainties in the numerical simulation is the non-intrusive polynomial chaos described in Crestaux and Martinez [22]. This method has been retained because of its reduced computational cost, good accuracy, and easy implementation (see, for instance, Congedo *et al*. [23] for an application to inviscid dense gas flows with multiple uncertainties) .

The flow configuration numerically studied in this work is derived from the experiments of Dellenback *et al*. [24], which have investigated the flow in an axisymmetric expansion for no-swirl and high-swirl inflow conditions. Measurements upstream of the expansion allow a proper description of the inflow statistics, and several measured velocity profiles downstream of the expansion provide a detailed picture of the flow development.

The paper is organized as follows: the physical and numerical details needed for a conventional deterministic analysis of RANS and LES solutions of the flow are reviewed in Section 2. The added information associated with UQ is described in Section 3 along with the UQ tools coupled with the available flow solvers; the accuracy of these tools is also checked. A detailed analysis of RANS and LES flow predictions subject to uncertain inlet conditions is presented in Section 4: both modeling approaches are critically assessed for flows with or without swirl.

2. CONVENTIONAL EXPERIMENT/SIMULATION COMPARISON

2.1. *Flow configuration*

The turbulent flow in a pipe with an axisymmetric expansion experimentally studied by Dellenback *et al*. [24] is considered for two main reasons: (i) it covers a variety of flow regimes, displaying recirculating flow regions and high turbulence levels; and (ii) it is a well-documented experiment allowing for a fine comparison between measurements and computations. This experiment has already been used by Schlüter *et al*. [25] as a reference for (deterministic) numerical simulations in a hybrid RANS/LES context and by Gyllenram and Nilsson [26] as a validation test case for a modified $k-\omega$ turbulence model. A sketch of the experimental configuration is given in Figure 1 where the plane generating the full geometry by rotation around the z-axis is displayed: the fluid is flowing from left to right, entering the pipe at $z = -2D$ with or without swirl, and leaving the

DOI: 10.1002/fld

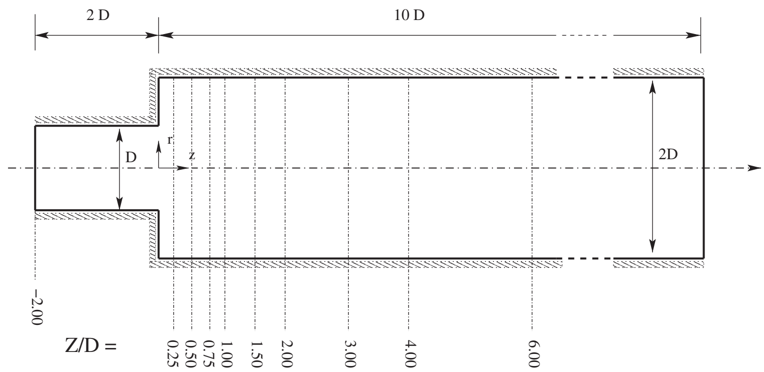

Figure 1. Experimental configuration of Dellenback.

expansion at $z = 10D$. Measurements with laser Doppler anemometer are available upstream of the expansion located in $z = 0$, allowing for a proper description of the mean inflow quantities such a time-averaged axial and tangential velocity. Available probe locations downstream the expansion are also indicated in Figure 1. This incompressible flow configuration is described by two non-dimensional parameters: the Reynolds number Re (based on the fluid kinematic viscosity, the inlet diameter D, and the bulk velocity U_b) and the swirl number S_w describing the level of swirl in the inlet flow. The swirl number is defined as the ratio between angular momentum flux and axial momentum flux:

$$S_w = \frac{1}{R} \frac{\displaystyle\int_0^R r^2 \langle u_z \rangle \langle u_\theta \rangle \, \mathrm{d}r}{\displaystyle\int_0^R r \langle u_z \rangle^2 \, \mathrm{d}r}, \tag{1}$$

where $R = D/2$, r is the radial coordinate (Figure 1) and $\langle u_z \rangle$, $\langle u_\theta \rangle$ denote respectively the time-averaged streamwise and tangential velocity components. The experiment is reported performed for a Reynolds number $Re = 30,000$ and two values of the swirl number: a no-swirl configuration ($S_w = 0$) and a strong swirl configuration ($S_w = 0.6$). The baseline flow (BF) configuration with a bulk velocity yielding $Re = 30,000$ and no swirl (NS) will be denoted from now on as BFNS test case; similarly, BFHS will denote the BF at $Re = 30,000$ with high swirl (HS) ($S_w = 0.6$).

2.2. *Turbulence modeling and numerical tools*

The incompressible turbulent flow considered in this study is governed by the instantaneous Navier–Stokes equations expressing mass and momentum conservation:

$$\begin{cases} \dfrac{\partial u_i}{\partial x_i} = 0, \\[2mm] \dfrac{\partial u_i}{\partial t} + \dfrac{\partial u_i u_j}{\partial x_j} = -\dfrac{1}{\rho} \dfrac{\partial p}{\partial x_i} + \dfrac{\partial}{\partial x_j} \left(\nu \dfrac{\partial u_i}{\partial x_j} \right), \end{cases} \tag{2}$$

where u_i, p, ρ, and ν are respectively the velocity components, the pressure, the (constant) density, and the kinematic viscosity. For high-level turbulent flows, it is not possible to perform DNS, that is, to solve directly these equations with the computing resources available, because of the too large range of fluid motion scales to account for. Some modeling of a part of the flow dynamics is needed to overcome this limitation. The RANS approach solves the mean flow and attempts to model the fluctuating field. The governing equations take the form as follows:

DOI: 10.1002/fld

$$
\begin{cases}
\dfrac{\partial \langle u_i \rangle}{\partial x_i} = 0, \\
\dfrac{\partial \langle u_i \rangle \, \langle u_j \rangle}{\partial x_j} = -\dfrac{1}{\rho} \, \dfrac{\partial \langle P \rangle}{\partial x_i} + \dfrac{\partial}{\partial x_j} \left((\nu + \nu_T) \dfrac{\partial \langle u_i \rangle}{\partial x_j} \right).
\end{cases} \tag{3}
$$

where $\langle u_i \rangle$ denotes the time-averaged velocity field components and $\langle P \rangle$ is the modified mean pressure. The influence of the fluctuations on the mean flow is described by the turbulent stress tensor $\nu_T \frac{\partial \langle u_i \rangle}{\partial x_j}$ with the turbulent viscosity ν_T to be modeled in order to close the system. Several standard turbulence models can be applied to define ν_T and perform RANS simulations [20]. In the present work, the standard $k - \epsilon$ model has been retained [27], where ν_T is expressed as a function of the turbulent kinetic energy k and the dissipation ϵ of this turbulent energy. These two additional turbulent quantities are themselves determined by solving transport equations that are not detailed here.

Alternatively, the LES approach proposes to solve only the filtered velocity field $\bar{u}_i$, where the filtering operation allows separation of the scales of the flow motion at the grid level, with the small motion scales taken into account by a subgrid-scale model. The filtered velocity field is computed as the solution of the filtered Navier–Stokes equations:

$$
\begin{cases}
\dfrac{\partial \bar{u}_i}{\partial x_i} = 0, \\
\dfrac{\partial \bar{u}_i}{\partial t} + \dfrac{\partial \bar{u}_i \, \bar{u}_j}{\partial x_j} = -\dfrac{1}{\rho} \, \dfrac{\partial \bar{P}}{\partial x_i} + \dfrac{\partial}{\partial x_j} \left((\nu + \nu_{SGS}) \dfrac{\partial \bar{u}_i}{\partial x_j} \right).
\end{cases} \tag{4}
$$

where the eddy viscosity ν_{SGS} must be defined to close system (4). The standard dynamic Smagorinsky model [28] will be used in this study: the eddy viscosity is computed as $\nu_{SGS} = (C \ \Delta)^2 \ \left| \bar{S}(x,t) \right|$, where $\left| \bar{S}(x,t) \right|$ is the norm of the filtered strain rate tensor. This expression defines ν_{SGS} algebraically so that no additional equation needs to be solved; the C coefficient is dynamically computed following Germano's definition [28].

The $k - \epsilon$ model is not necessarily the best choice for an accurate RANS computation of the flow under study, and the dynamic Smagorinsky model is not the sole choice of subgrid model. Let us emphasize, however, that our objective is not to investigate the accuracy of RANS modeling with respect to LES but to assess the comparative behavior of both approaches when uncertainties are introduced in the flow description. In this respect, the $k - \epsilon$ model on the one hand and the dynamic Smagorinsky model on the other hand, which are commonly used models, remain valid choices.

Both RANS and LES approaches have been used as implemented into the open source finite volume code OpenFOAM[‡]. In systems (3) and (4), convective and viscous fluxes are discretized with a second-order accurate central differencing scheme. The pressure–velocity coupling is insured by using the Pressure Implicit with Splitting of Operators (PISO) algorithm [29]. To avoid spatial oscillations of the pressure field over the collocated grid arrangement, Rhie and Chow pressure-weighted interpolation is applied [30]. Moreover, for system (4), time advancement is performed by using a Crank–Nicholson scheme.

For RANS steady simulations, the outflow boundary condition is based on extrapolation conditions that require that the derivatives of all quantities in the direction normal to the boundary be zero. However, this condition is known to be not satisfactory in unsteady flows [31]. A convective outflow condition [32] is thus used for LES unsteady simulations.

For both RANS and LES computations, the profiles of the time-averaged streamwise and ortho-radial velocities are imposed at the inlet boundary from the measured data of Dellenback *et al.* [24]. These profiles depend on the bulk velocity U_b and the swirl number S_w. Because the first measure point in the inlet section is located outside the boundary layer, the imposed velocity profiles are smoothly connected to the zero value at the wall by a zero-pressure gradient turbulent boundary layer velocity distribution.

[‡]www.openfoam.com

DOI: 10.1002/fld

When the LES approach is applied, the time-averaged profile must be completed with a time-dependent disturbance. Such a perturbation is used to allow the flow instabilities development in LES unsteady computations. In this work, the time-dependent inlet velocity distribution is defined with a white noise as follows:

$$\bar{u}_{i,\mathrm{LES}}(t) = \langle u_{i,\mathrm{EXPE}} \rangle (U_b, S_w) + \gamma_i \sqrt{\frac{2}{3}\, k_i}, \tag{5}$$

where $\langle u_{i,\mathrm{EXPE}} \rangle$ is the experimental time-averaged velocity depending on U_b and S_w, k_i is the inlet turbulent kinetic energy, and γ_i is a sequence of random numbers conditioned so that each distribution has zero mean and unit variance. Various more complex methods have been proposed to impose this time-dependent perturbation [33–35]. However, it was decided in this work to focus the analysis on a perturbation based on a white noise method only because this is the simplest and most commonly used method so that the conclusions drawn regarding the impact of inflow uncertainties benefit to the largest basis of LES practitioners. The inlet boundary condition with white noise, Equation (5), is only applied to the BFNS configuration. Indeed, strongly swirling flows are known to allow self-sustained instabilities without a significant influence of the initial disturbance. On the same test case, Schlüter *et al.* [25] have previously demonstrated that inlet turbulent fluctuations can be neglected when strong swirl is considered. In the present study, preliminary deterministic LES computations for BFHS have been performed using the previously described numerical tools without and with inflow perturbation, leading to similar predictions for the velocity profiles of interest. It was thus decided to define the LES inlet boundary condition by the simple relationship $\bar{u}_{i,\mathrm{LES}}(t) = \langle u_{i,\mathrm{EXPE}} \rangle$ for BFHS.

When the RANS approach is used, the condition $\langle u_{i,\mathrm{RANS}} \rangle = \langle u_{i,\mathrm{EXPE}} \rangle$ is systematically used. However, additional inlet conditions have to be defined for the additional transport equations of k and ϵ. The inlet value of k and ϵ are computed from the bulk velocity U_b and estimated values of the turbulence intensity T_i and the characteristic turbulence length scale L_t, following the classical relations:

$$k = \frac{3}{2}\ (T_i\ U_b)^2 \quad \epsilon = \frac{k^{3/2}}{L_t}, \tag{6}$$

In conclusion, the RANS inlet boundary condition depends on a set of four physical parameters: U_b, S_w, T_i, and L_t. The LES inlet boundary condition solely depends on U_b and S_w for BFHS and also depends on T_i for BFNS. For BFNS and BFHS, $U_b = 0.452\, m/s$ corresponds to $Re = 30,000$ and $S_w = 0$ or $S_w = 0.6$. The turbulence intensity T_i is estimated equal to 0.03, leading to velocity fluctuation about 3% of the bulk velocity, and the turbulence characteristic length scale L_t equal to 5% of the inlet radius. Note that these quantities are rarely available from experimental data, and there are no well-established rules to determine their values. This is an additional motivation to quantify uncertainties on the results due to uncertainties on such inlet levels.

2.3. *Mesh convergence study*

A conventional experiment/simulation comparison would first focus on finding the optimal grid resolution that ensures grid-independent numerical results (or at least a remaining level of grid dependence below a prescribed threshold) while minimizing the cost of the numerical simulation. The available experimental results are typically used as target values in this process. Once grid independence is achieved, the numerical solver is usually applied to deepen the physical understanding of the flow under study (each grid cell being used as a probe) or to perform a parametric study around the experimental baseline configuration. In the present work, the analysis will be focused on the comparison between experiment and simulation when the physical uncertainties found in the experiment are injected in the numerical simulation. As will be next detailed, this more involved but also more realistic comparison requires to perform a set of flow computations, each of them being grid-converged. The mesh convergence study is performed for the BFHS configuration computed with the LES approach because this combination is the most demanding as far as grid resolution is concerned. The time-averaged axial and tangential velocity profiles measured in the experiment are

DOI: 10.1002/fld

compared with time-averaged profiles computed by LES on a series of increasingly refined grids (Figures 2 and 3): a coarse grid containing $880,000$ cells with $y^+ = 5$ for the first grid point next to the wall boundary, a medium grid of $1,500,000$ cells with $y^+ = 2$, and a fine grid of $5,600,000$ cells with $y^+ = 0.5$. Because the plotted values of velocity at section z/D in Figures 2 and 3 are shifted by a factor $4z/D$ with respect to their actual computed or measured values for an improved readability of the plots, the velocity distribution at a given section is directly read as the difference between these plots and the vertical dotted line associated with each section. It can be observed in Figure 2 that the swirl leads to the formation of an extended back-flow region downstream of the expansion, associated with high shear levels. The numerical results on the three grids and the experimental data are globally in good agreement, with a well-predicted back-flow region. However, the coarse grid yields a slightly over-predicted velocity peak for U_z immediately outside the recirculation region (in the radial direction), which leads in turn to a shorter recirculation zone well visible at $z/D = 1$. The fine and medium grids yield very similar mean axial velocity profiles all along the expansion. The mean tangential velocity profiles plotted in Figure 3 seem even less sensitive to the grid coarsening with an already good overall agreement between computation and experiment on the coarse grid. This grid convergence study leads us to retain the medium grid for all subsequent computations. It will be a posteriori checked if the observed differences between the medium and fine grid computations will remain negligible with respect to the variations introduced in the next section by taking into account inflow uncertainties.

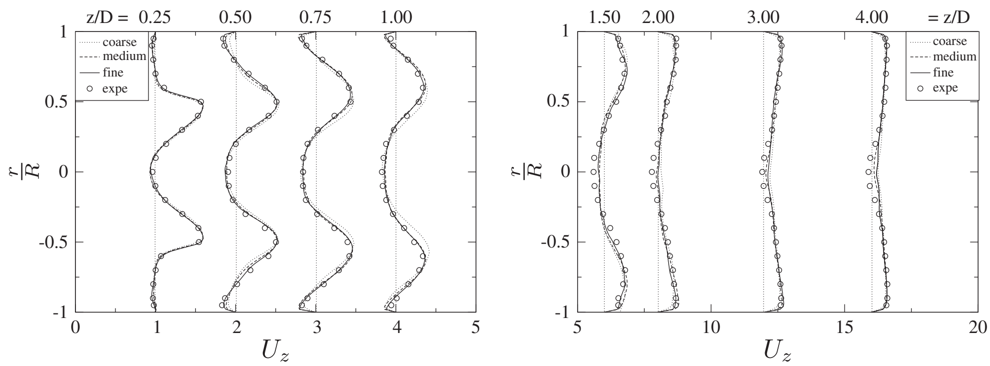

Figure 2. Baseline flow with high swirl configuration. Mean axial velocity profiles computed at different streamwise sections on the coarse, medium, and fine grids using the large-eddy simulation approach. Comparison with the experimental measurements taken from Dellenback *et al*. [24]. Note that the velocities at section z/D are systematically shifted by a value $4\,z/D$ with respect to their actual values to avoid superimposed plots.

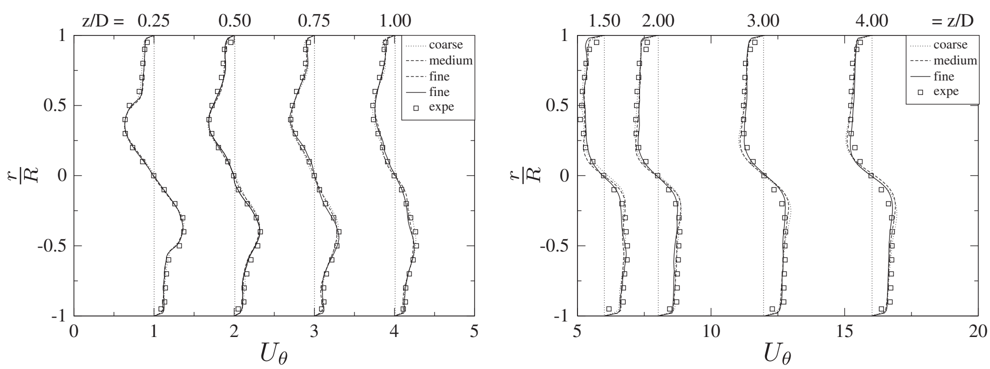

Figure 3. Baseline flow with high swirl configuration. Mean tangential velocity profiles computed at different streamwise sections on the coarse, medium, and fine grids using the large-eddy simulation approach. Comparison with the experimental measurements taken from Dellenback *et al*. [24]. Note that the velocities at section z/D are systematically shifted by a value $4\,z/D$ with respect to their actual values to avoid superimposed plots.

DOI: 10.1002/fld

3. EXPERIMENT/SIMULATION COMPARISON INCLUDING UNCERTAINTIES

3.1. Setting up the uncertainties

The calculations performed in the previous section assumed exactly known inlet flow conditions when using the RANS or LES numerical modeling; the grid-converged computed results were then compared with measured quantities also assuming exactness of the measurements. In reality, the measured distributions reported in Dellenback *et al*. [24] must be considered as averaged distributions over a set of experimental realizations. From one realization to another, the inlet bulk velocity U_b and swirl number S_w (for the BFHS configuration) are subject to a level of fluctuation, which lead in turn to some fluctuations in the velocity measurements. We will consider from now on $\overline{U_b} = 0.452$ m/s and $\overline{S_w} = 0.6$ (for BFHS) to be mean values around which actual values of U_b and S_w in the series of experiments are uniformly distributed. In other words, U_b and S_w are now stochastic variables described by uniform probability distribution functions (PDFs) over the respective intervals $[0.975\,\overline{U_b}, 1.025\,\overline{U_b}]$ and $[0.975\,\overline{S_w}, 1.025\,\overline{S_w}]$. The choice of a 2.5% variance for both U_b and S_w is based on the analysis of the experimental setup description provided by Dellenback *et al*. [24]. The inlet turbulence characteristics are also subject to uncertainty. However, because no information is available in Dellenback *et al*. [24] regarding these quantities, the extent of variation for T_i and L_t was estimated from previous calculations on similar configurations [36–38]. The turbulence intensity T_i is assumed to vary between 0.006 and 0.06 following a uniform PDF; that is, the velocity fluctuation is assumed to vary uniformly between 0.6% and 6% of the mean velocity; the characteristic turbulence length scale is assumed to vary between 0.1% and 10% of the inlet radius R, following a uniform PDF.

The uncertainty on U_b impacts all the simulations through the inlet velocity boundary condition: with or without swirl, using RANS or LES approach. The uncertainty on S_w impacts the simulations with swirl only, as S_w is assumed to remain very close to zero (with a negligible uncertainty) for the configuration without swirl. The uncertainty on T_i impacts all the RANS calculations through the inlet boundary condition (6) for k and ϵ and the LES calculation for the configuration without swirl through the inlet boundary condition (5). The uncertainty on L_t impacts all the RANS calculations through the inlet boundary condition (6) for ϵ but does not play a role in the LES calculations. The uncertainties taken into account in the study are summarized in Table I. It remains to analyze how these physical (U_b, S_w) and modeling (T_i, L_t) uncertainties impact the numerical solutions provided by the RANS and LES approaches.

3.2. Tools for uncertainty quantification

Let us consider a stochastic differential equation of the following form:

$$L\,(\mathbf{x}, \theta, \phi) = f\,(\mathbf{x}, \theta) \tag{7}$$

where L is a non-linear spatial differential operator (for instance, L is the RANS operator defined by (3)), θ is a random vector whose dimension depends on the number of uncertain parameters in the problem, and $f(\mathbf{x}, \theta)$ is a source term depending on the position vector $\mathbf{x}$ and on θ. The solution of the stochastic Equation (7) is the variable $\phi(\mathbf{x}, \theta)$ depending on the space variable $\mathbf{x} \in \mathbf{R}^d$ and on θ. Under specific conditions, a stochastic process can be expressed as a spectral expansion based on suitable orthogonal polynomials, with weights associated with a particular probability

Table I. Considered uncertainties for the various computations.

Simulations	U_b (m/s)	S_w	T_i	L_t
RANS with swirl	0.452 ± 0.0113	0.6 ± 0.015	0.006 to 0.06	0.1%R to 10% R
RANS without swirl	0.452 ± 0.0113	/	0.006 to 0.06	0.1%R to 10% R
LES with swirl	0.452 ± 0.0113	0.6 ± 0.015	/	/
LES without swirl	0.452 ± 0.0113	/	0.006 to 0.06	/

RANS, Reynolds-averaged Navier–Stokes; LES, large-eddy simulation.

DOI: 10.1002/fld

density function. The basic idea is to project the variables of the problem onto a stochastic space spanned by a complete set of orthogonal polynomials Ψ that are functions of random variables $\xi(\theta)$, where θ is a random event [22, 23, 39–41]. For example, the unknown variable ϕ has the following spectral representation:

$$\phi(\mathbf{x}, \theta) = \sum_{i=0}^{\infty} \phi_i(\mathbf{x}) \Psi_i(\xi(\theta)) \tag{8}$$

In practice, the series in Equation (8) has to be truncated to a finite number of terms, here denoted with N. The total number of terms of the series is determined by the following:

$$N + 1 = \prod_{k=1}^{n} (p_k + 1) \tag{9}$$

where n is the dimensionality of the uncertainty vector θ, and p_k is the order of the expansion polynomial associated to the kth random variable. Substituting the polynomial chaos expansion (8), into the stochastic differential Equation (7), we obtain the following:

$$L\left(\mathbf{x}, \theta; \sum_{i=0}^{N} \phi_i(\mathbf{x}) \Psi_i(\xi(\theta))\right) = f(\mathbf{x}, \theta) \tag{10}$$

Equation (10) is solved through the weighted residual method. The collocation method is obtained by choosing Dirac-delta weighting functions. The coefficients $\phi_i(\mathbf{x})$ are obtained using quadrature formulae based on tensor product of a 1D formula. Applying a collocation projection to Equation (10), we obtain the solution of a deterministic problem for each collocation point. In both cases, once the chaos polynomials and the associated ϕ_i coefficients have been determined, the expected value and the variance of the stochastic solution $\phi_i(\mathbf{x}, \theta)$ are computed from the following:

$$E_{PC} = \phi_0(\mathbf{x}) \tag{11}$$

$$\mathrm{Var}_{\mathrm{PC}} = \sum_{i=1}^{N} \phi_i^2(\mathbf{x}) \left\langle \Psi^2 \right\rangle \tag{12}$$

Another interesting property of PC expansion is to make easier sensitivity analysis based on the analysis of variance (ANOVA) decomposition. By decomposing variance, we can compute variance introduced by interactions of random variables and variance generated by a given random variable only. For further details, see Refs. [22, 23, 42, 43].

3.3. Coupling computational fluid dynamics and uncertainties quantification

The non-intrusive stochastic method used in this study allows evaluating the flow statistics when some of the inlet parameters are uncertain by performing a series of deterministic computations with specific fixed values for the uncertain parameters—also defined as stochastic design of experiments (DOE). The CFD solvers previously used in Section 2 remain unchanged. Once the deterministic realizations are performed, their results are used to compute statistics of the solution by means of Equations (11) and (12). The cost of the UQ process is essentially proportional to the size of the stochastic DOE as the computational cost of the flow statistics is negligible with respect to the unit cost of a single CFD realization, be it with a RANS or with a LES approach. The size of the stochastic DOE is equal to $(p+1)^n$ for the non-intrusive polynomial chaos approach used in this work, where n is the number of uncertain parameters taken into account and p the order of the polynomial chaos. For reasons that will be explained in the next paragraph, second-order and third-order Legendre polynomial chaos have been considered (referred to as PC(2) and PC(3) from now on)—Legendre polynomials are retained as we are dealing with uniform PDF for the uncertain variables. When the RANS approach is applied to the configuration with swirl, four uncertainties are considered, which means that 25 computations have to be performed when PC(2) is used to compute the

DOI: 10.1002/fld

flow statistics and 125 computations are needed when PC(3) is used. When the RANS approach is used for the configuration without swirl, the number of uncertainties reduces to 3 so that 16 (respectively 64) computations are needed to compute the flow statistics using PC(2) (respectively PC(3)). When LES is used for the flow configuration with or without swirl, only two uncertainties have to be taken into account, yielding nine LES computations when PC(2) is used to evaluate the flow statistics. In terms of computational cost, one iteration of RANS simulation has roughly the same cost as the LES approach. However, the physical analysis performed in Section 3 will be focused on time-averaged quantities. Indeed, the analysis of instantaneous quantities was not considered first of all for lack of experimental data; note also that polynomial chaos could introduce convergence issues when dealing with unsteady flow problems (for instance, Orzag and Bissonette [44]). These time-averaged quantities are directly provided by the steady RANS approach, whereas they have to be computed from various iterations when the flow is well established in the case of the LES approach. It has been established for the present simulations that the computational cost to provide time-averaged quantities is roughly 60 times more important for LES than for RANS. The overall cost of the RANS stochastic analysis is consequently between 16 and 125 times the computational cost of one deterministic RANS simulation, whereas this cost for the LES stochastic analysis is around 540 (9×60) times the computational cost of one deterministic RANS simulation. In this work, this cost has been optimized by making use of domain decomposition and parallel computing with Message Passing Interface (MPI) based exchange of information between the different grid blocks and by performing in parallel the decoupled deterministic computations of the stochastic DOE.

3.4. Convergence analysis of the uncertainty quantification

The next section will be entirely dedicated to the physical analysis of the computed RANS and LES flows in the presence of uncertain inlet conditions and to the comparison of these flow statistics with the experimental results including measurement errors. Before performing this analysis, however, a trade-off must be found between the accuracy of the computed statistics and the overall computational cost of the stochastic DOE. To this end, PC(2) and PC(3) are applied to the configurations with and without swirl computed with the RANS approach, and an ANOVA analysis is performed using the statistics obtained from the PC(2) DOE and the PC(3) DOE. These statistics allow for instance the computation of the variance of the time-averaged velocity magnitude at each grid point; the maximum value $\sigma_{\max}$ taken by this variance over the computational grid is reported in Table II for PC(2) and PC(3), along with the computed contribution to this variance for each uncertain parameter (σ_{U_b} for the contribution of U_b to the maximum total variance, and so on).

It can be checked that the prediction of the maximum variance of the velocity magnitude is only slightly modified (by 3.6% for the flow with swirl and 2.8% for the flow without swirl) when using PC(3) instead of PC(2). Note that the location of the maximum variance in the computational grid is also the same for PC(2) and PC(3). Moreover, the hierarchy of the most influential parameters is identical for PC(2) and PC(3) with little differences on the relative contribution of each uncertain parameter to the total variance. A PC(4) analysis for the high-swirl configuration with RANS and four inlet uncertainties would require a stochastic DOE of size 625, which appears as an unnecessarily expensive verification step for the convergence of the UQ process. A much cheaper

Table II. Computed PC(2) and PC(3) statistics for Reynolds-averaged Navier–Stokes stochastic simulations.

	$\sigma_{\max}$	σ_{U_b} (%)	σ_{S_w} (%)	σ_{T_i} (%)	σ_{L_t} (%)
Flow with swirl/PC(2)	0.0146	0.81	0.50	95.9	2.31
Flow with swirl/PC(3)	0.0151	0.82	0.53	96.2	2.15
Flow without swirl/PC(2)	0.000897	9.0	/	39.9	50.7
Flow without swirl/PC(3)	0.000923	8.9	/	39.7	51.1

Maximum variance $\sigma_{\max}$ of the time-averaged velocity magnitude and contribution (in %) of each source of uncertainty to this maximum variance.

DOI: 10.1002/fld

verification can be performed by taking advantage of the contributions to the variance reported in Table II. Indeed, because the turbulence intensity T_i appears to be the most influential uncertain inflow parameter for the high-swirl flow configuration, it is decided to compute the mean flow and its variance when this single inflow parameter is left uncertain; in that case, the size of the stochastic DOE is limited respectively to 8, 16, and 32 for PC(3), PC(4), and PC(5), which makes the convergence study truly affordable. It has been found that the L_2 norm of the variance of the computed velocity fields displays a maximum variation of 1% when using PC(4) instead of PC(3). Once this additional confidence in the results computed using PC(3) is obtained, it is decided to perform in the next section the physical analysis of the flow, including the whole set of uncertain inflow parameters, on the basis of the PC(3) solutions.

The same convergence analysis, using PC(2) and PC(3), could be performed with the LES approach. However, the polynomial chaos method is known to converge rapidly when steady non-shocked flows are considered [17], which is the case of the present study; moreover, this property has been confirmed by the previous RANS analysis. Consequently, the LES flow prediction in the presence of uncertain parameters will be analyzed in the next section on the basis of PC(2) and a stochastic DOE of size 9. Note also that the relative differences between RANS and LES predicted variance using PC(2) will be much larger than the relative difference between PC(2) and PC(3) for the RANS computations.

Note that the choice of uniform PDF for the uncertain inflow parameters is rather arbitrary; it is mainly motivated by the lack of available physical data for guiding the choice of a specific PDF. In order to assess the impact of the postulated distributions on the stochastic output, a UQ analysis based on a PC(5) with a Gaussian PDF for the inflow turbulence intensity retained as the single uncertain parameter was performed and its results compared with those given by PC(5) and a uniform PDF for T_i. When analyzing the L_2 norms of the mean fields and the variance fields for each velocity component, computed either for a uniform or a Gaussian PDF, it was found that the norms of the mean field were almost equal, whereas the computed norms of the variance with a uniform PDF are about 2.5 greater than those computed with a Gaussian PDF. As the present exploratory study wishes to emphasize the need to take into account uncertain inflow conditions when performing RANS or LES flow computations, the choice of uniform PDFs increasing the sensitivity of the numerical results to the inflow uncertainties seems appropriate.

4. ANALYSIS OF REYNOLDS-AVERAGED NAVIER–STOKES AND LARGE-EDDY SIMULATION FLOW PREDICTIONS

The accuracy of both the flow simulations and the stochastic analysis having been established, it is now possible to analyze the RANS and LES flow predictions when physical and modeling uncertainties on the inlet conditions are taken into account.

4.1. High-swirl configuration

Figure 4 displays the central plane of the flow colored by the mean time-averaged axial velocity computed using the RANS computations and PC(3). The basic qualitative pattern of the mean flow

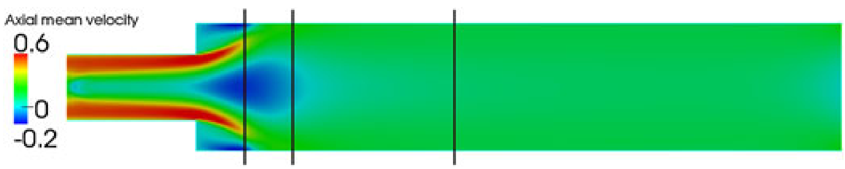

Figure 4. High-swirl flow. Reynolds-averaged Navier–Stokes computations analyzed using PC(3). Mean-value contours (ms^{-1}) of the time-averaged velocity magnitude. Vertical lines correspond to the sections used for the comparison with experiment (Figures 5 and 6).

DOI: 10.1002/fld

is similar to that observed in Section II for BFHS on the streamwise sections plotted in Figure 2, with in particular a recirculation zone occurring around the flow centerline downstream of the expansion zone.

4.1.1. Comparison with experiment. Experimental measurements and simulation results are now compared, taking into account the measurement errors and the propagation of uncertainties on the inlet flow conditions in the numerical simulations as detailed in Table I. Figure 5 reports the experimental, RANS, and LES axial mean velocity distributions along the radial coordinate in several transversal sections, where error bars indicate the computed variance of the numerical solutions (using PC(3) for the RANS results and PC(2) for the LES results) and the experimental error. A tentative estimation of the error levels associated with the measurement instruments used at the time of the experiment (1987) led us to assume the measurement error on the local velocity values to be consistently equal to ± 0.04 m/s, be it in the inlet section or at any downstream location. Three sections have been considered (Figure 1), located respectively near the expansion ($L/D = 0.75$), in the center of the computational domain ($L/D = 1.5$), and near the exit ($L/D = 4.0$).

Let us emphasize again that the plots previously displayed in Figure 2 were limited to the comparison between experimental data and LES simulations performed for a single set of values of the inlet flow conditions (equal to the mean values of these quantities) with supposedly exact measured values. The present analysis provides a more realistic assessment of the predictive properties of the RANS and LES approaches as the stochastic DOE for U_b, S_w, T_i, and L_t reproduces the actual variability of the inlet flow conditions encountered in the experiment. Ideally, when the inlet flow conditions follow the statistical description summarized in Table I, the mean numerical solution should be close to the reported (mean) experimental distribution with a variance associated with the numerical results similar to the estimated experimental error.

When using RANS modeling, the mean axial velocity curves remain systematically far from the experimental distributions (Figure 5(a)–(c)). This observation is consistent with the well-known fact

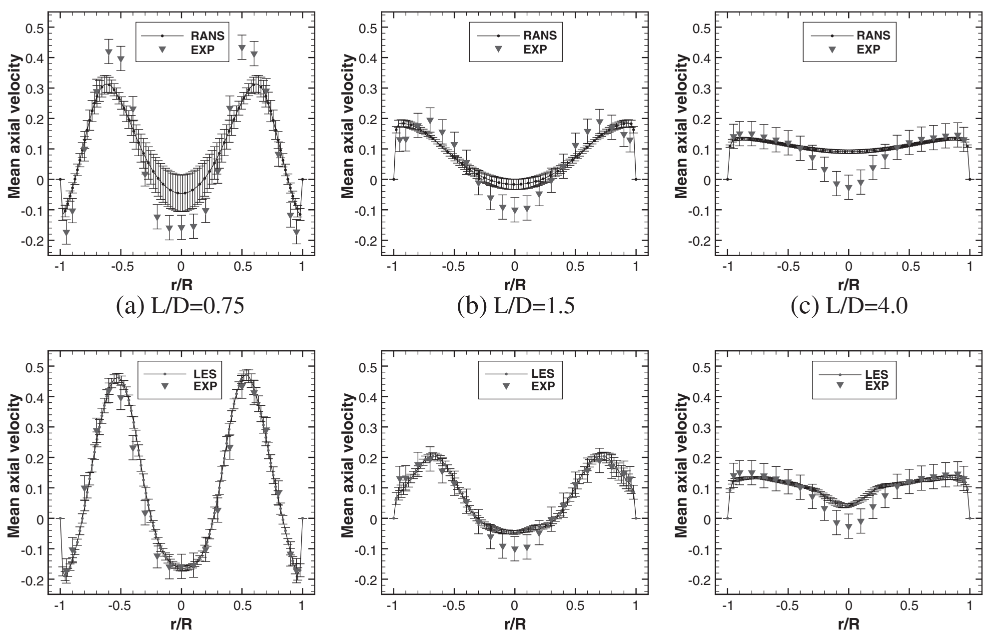

(a) L/D=0.75 (b) L/D=1.5 (c) L/D=4.0

(d) L/D=0.75 (e) L/D=1.5 (f) L/D=4.0

Figure 5. High-swirl flow. Statistics of the axial velocity distributions (mean value and standard deviation displayed as error bar) at successive sections (from left to right: upstream to downstream) computed with Reynolds-averaged Navier–Stokes modeling/PC(3) (top: a, b, c) and large-eddy simulation modeling/PC(2) (bottom: d, e, f). Numerical results are compared with experimental measurements (mean value and assumed experimental error bar).

DOI: 10.1002/fld

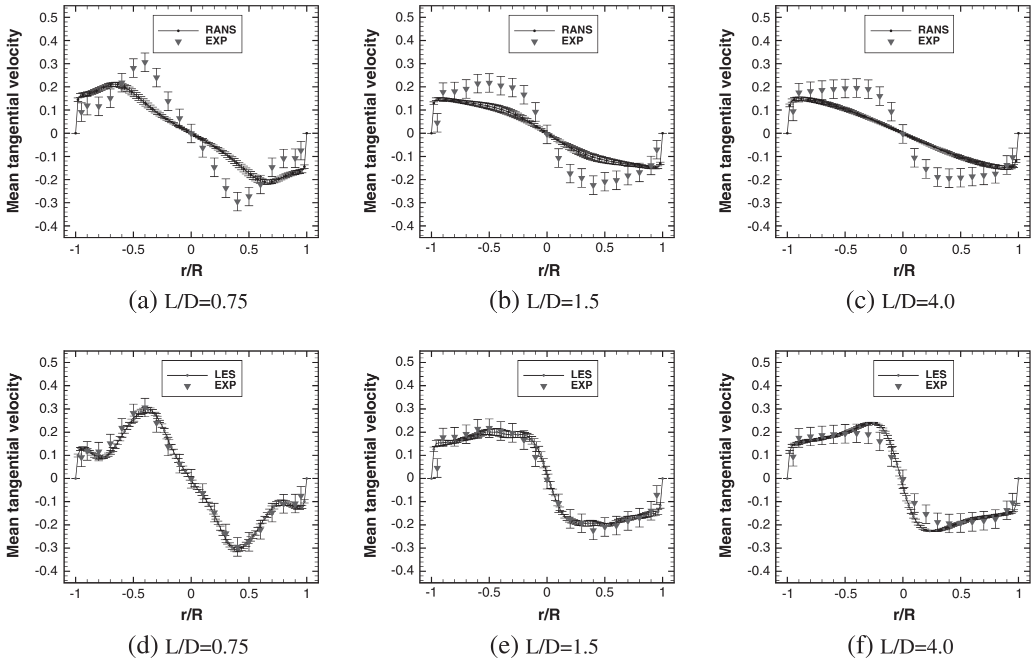

(a) L/D=0.75 (b) L/D=1.5 (c) L/D=4.0

(d) L/D=0.75 (e) L/D=1.5 (f) L/D=4.0

Figure 6. High-swirl flow. Statistics of the tangential velocity distributions (mean value and standard deviation displayed as error bar) at successive sections (from left to right: upstream to downstream) computed with Reynolds-averaged Navier–Stokes modeling/PC(3) (top: a, b, c) and large-eddy simulation modeling/PC(2) (bottom: d, e, f). Numerical results are compared with experimental measurements (mean value and assumed experimental error bar).

that the turbulent-viscosity assumption leads to inaccurate flow patterns for strong swirling flows. Furthermore, the computed error bars at section $L/D = 0.75$ in the back-flow region close to the centerline $r/R = 0$ (Figure 5 (a)) are much larger than the 2.5% inlet velocity uncertainty, indicating the strong sensitivity of the RANS approach. These computed error bars tend to reduce rapidly for more downstream sections as they are of the same order as the measurement error bars (assumed consistently equal to the input uncertainty) for $L/D = 1.5$ and smaller for $L/D = 4.0$ but with a computed mean distribution largely overestimated near the flow centerline. When using LES modeling, the picture is quite different as the mean solution is globally in good agreement with the measured distribution, *and* the numerical error bars remain similar or even smaller than the experimental error bars in all the sections under study (Figure 5(d)–(f)).

A similar analysis can be performed for the time-averaged tangential velocity distributions and the computed mean values and variance distributions at the same sections $L/D = 0.75$, 1.5, and 4 are reported in Figure 6. As observed in Figure 6(a)–(c), the error bars for the RANS prediction remain small, inferior to the experimental error. The computed mean distribution remains, however, systematically far from the measured profile. The RANS approach can be considered as unable to correctly predict the physical flow solution on the basis of a full analysis including the uncertainties on the inlet flow conditions. It must also be noted that these physical uncertainties have specifically a great impact on the numerical prediction of the axial velocity in recirculating flow regions.

When using the LES approach, the errors bars on tangential are also small but with a computed mean solution that remains systematically close to the experimental profiles (Figure 6(d)–(f)).

4.1.2. Explanation of variance. Because mean flow quantities and their variance are computed at each grid point, it is possible to plot the contours of the variance field for the time-averaged velocity magnitude in order to better understand how the computed uncertainties are spatially distributed in the flow. This analysis will be performed for the RANS approach only because the uncertainties associated with the LES approach were found to remain small. The variance contours plotted in

DOI: 10.1002/fld

Figure 7 indicate that the highest values for the variance of the time-averaged velocity magnitude are correlated with the location of the back-flow region well visible in Figure 4. Moreover, ANOVA analysis can be applied at each grid point to estimate the contribution of each uncertainty to the global variance, and the contours of these uncertainty contributions can be plotted and analyzed. Such a process is successively applied to the four uncertainties taken into account when applying RANS modeling to the high-swirl configuration. The contours of T_i uncertainty contribution to the variance are plotted in Figure 8: they are very similar to the contours of the global variance plotted in Figure 8, which indicates that the global variance of the RANS computations is essentially produced by the uncertainty on inlet turbulence intensity. The contours of U_b, S_w, and L_t uncertainty contributions to the variance of the time-averaged velocity magnitude are respectively plotted in Figures 9–11 and illustrate the very weak contribution to the global variance of the uncertainty on bulk velocity, swirl number, and turbulence length scale.

Figure 7. High-swirl flow. Reynolds-averaged Navier–Stokes computations analyzed using PC(3). Variance contours (m^2 s^{-2}) of the time-averaged velocity magnitude.

Figure 8. High-swirl flow. Reynolds-averaged Navier–Stokes computations analyzed using PC(3). Contours of T_i uncertainty contribution to the variance of the time-averaged velocity magnitude.

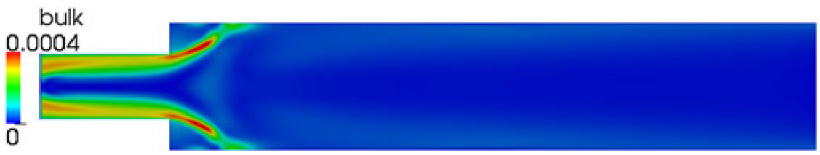

Figure 9. High-swirl flow. Reynolds-averaged Navier–Stokes computations analyzed using PC(3). Contours of U_b uncertainty contribution to the variance of the time-averaged velocity magnitude.

Figure 10. High-swirl flow. Reynolds-averaged Navier–Stokes computations analyzed using PC(3). Contours of S_w uncertainty contribution to the variance of the time-averaged velocity magnitude.

Figure 11. High-swirl flow. Reynolds-averaged Navier–Stokes computations analyzed using PC(3). Contours of L_t uncertainty contribution to the variance of the time-averaged velocity magnitude.

DOI: 10.1002/fld

4.2. *No-swirl configuration*

Figure 12 displays the mean-value contours of the time-averaged axial velocity for the no-swirl configuration computed using the RANS approach and PC(3). With respect to the previously studied configuration, the absence of swirl yields a higher velocity in the centerline region of the flow; note also that back-flow regions appear close to the wall immediately downstream of the expansion.

4.2.1. Comparison with experiment. As already done for swirling flows, the experimental profiles of the time-averaged axial velocity are plotted in Figure 13 along with the mean values of the computed distributions using RANS and LES modeling; the experimental and computed standard deviations are also reported on the same plots. Let us recall that the error bar for the local velocity components measurement is systematically assumed equal to ± 0.04 m/s. Three sections, where experimental data are available, have been considered (Figure 1), respectively near the inlet ($L/D = -0.50$), in the center of the flow domain ($L/D = 1.0$), and near the exit ($L/D = 3.0$). The measured value at centerline $r/R = 0$ in section $L/D = 1$ is reported but seems spurious when compared with the other nearby measured values in the same section; it will be discarded in the following comments.

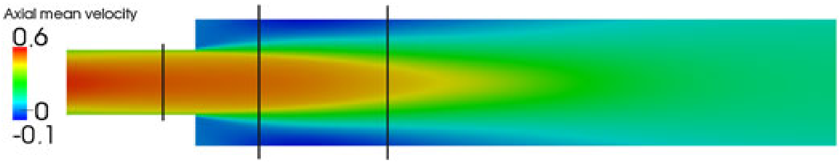

Figure 12. No-swirl flow. Reynolds-averaged Navier–Stokes computations analyzed using PC(3). Mean-value contours (ms^{-1}) of the time-averaged axial velocity. Vertical lines correspond to the sections used for the comparison with experiment (Figure 13).

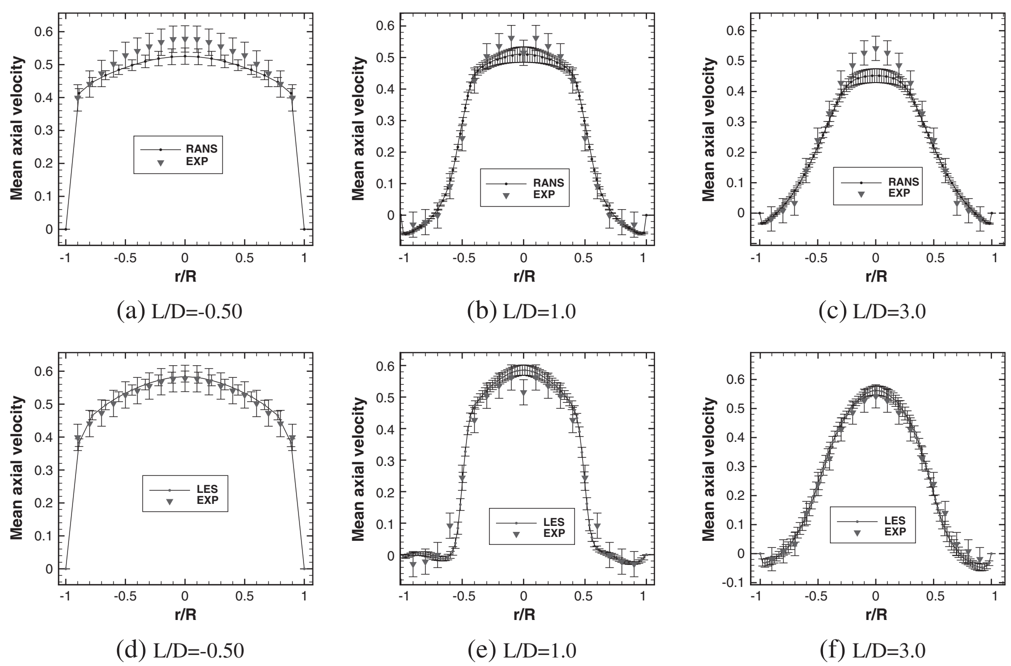

Figure 13. No-swirl flow. Statistics of the axial velocity distributions (mean value and standard deviation displayed as error bar) at successive sections (from left to right: upstream to downstream) computed with Reynolds-averaged Navier–Stokes modeling/PC(3) (top: a, b, c) and large-eddy simulation modeling/PC(2) (bottom: d, e, f). Numerical results are compared with experimental measurements (mean value and assumed experimental error bar).

DOI: 10.1002/fld

When the mean curves computed with RANS modeling are compared with measurements, taking into account their respective error bars, a correct agreement is found between experiment and computation. RANS modeling tends to underpredict, in the mean, the values of axial velocity near the centerline $r/R = 0$ and to slightly overpredict these values near the walls. However, the upper limit of the computed envelope near the centerline is located inside the region bounded by the lower and upper limits of the measured envelope at section $L/D = -0.50$ and $L/D = 1$; this same upper limit of the computed envelope remains slightly below the lower limit of the measured envelope in the downstream section $L/D = 3.0$. In contrast with the previous high-swirl configuration, the variation of the error bars between the far upstream and far downstream sections remains very small.

The LES prediction is also in very good agreement with the experiments (Figure 13(d)–(f)). LES modeling tends to slightly overpredict, in the mean, the axial velocity near the centerline. However, the upper limit of the computed envelope in this centerline region tends to coincide with the upper limit of the measured envelope. Moreover, the computed error bars for LES are sufficiently small for the numerical envelope to be almost fully included into the measured envelope for the three sections under study.

4.2.2. Explanation of variance. The variance contours of the velocity magnitude in the central plane of the pipe are plotted in Figure 14 for RANS computations. The maximum value reached by this variance remains well below the previously computed level for the high-swirl configuration (0.0009 against 0.015 $\mathrm{m}^2\ \mathrm{s}^{-2}$). Moreover, this variance reaches its maximum well downstream from the expansion, whereas this maximum was located in the immediate neighborhood of the expansion for the high-swirl case (Figure 7). The contours of the various contributions to this global variance are also reported in Figures 15–17. In contrast with the high-swirl case where the inlet turbulence intensity T_i explained most of the variance, the uncertainties on U_b, L_t, and T_i are all significantly contributing to the global variance in this no-swirl case. The uncertainty on bulk velocity explains most of the variance in the inlet region, whereas the downstream peak of the global variance is explained mostly by the uncertainties on the inlet turbulence intensity and turbulence characteristic length scale.

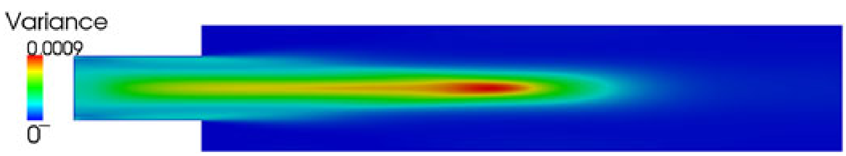

Figure 14. No-swirl flow. Reynolds-averaged Navier–Stokes computations analyzed using PC(3). Variance contours ($\mathrm{m}^2\ \mathrm{s}^{-2}$) of the time-averaged velocity magnitude.

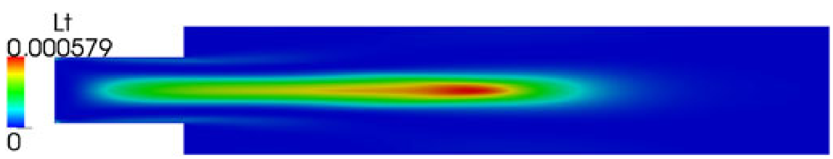

Figure 15. No-swirl flow. Reynolds-averaged Navier–Stokes computations analyzed using PC(3). Contours of L_t uncertainty contribution to the variance of the time-averaged velocity magnitude.

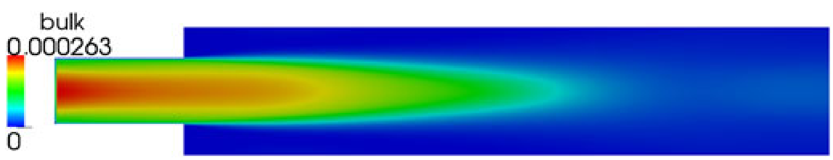

Figure 16. No-swirl flow. Reynolds-averaged Navier–Stokes computations analyzed using PC(3). Contours of U_b uncertainty contribution to the variance of the time-averaged velocity magnitude.

DOI: 10.1002/fld

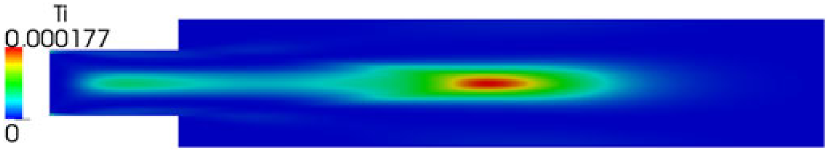

Figure 17. No-swirl flow. Reynolds-averaged Navier–Stokes computations analyzed using PC(3). Contours of T_i uncertainty contribution to the variance of the time-averaged velocity magnitude.

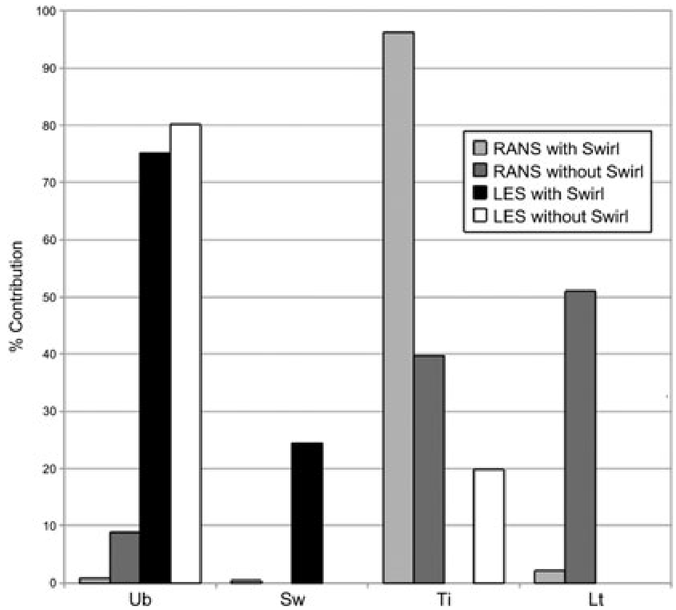

Figure 18. High-swirl/no-swirl flows. Analysis of the contributions to the maximal variance of the time-averaged velocity magnitude computed using RANS/PC(3) and LES/PC(2).

A summary of the ANOVA analysis is proposed in Figure 18 where the contributions to the maximum variance of the velocity magnitude are reported for the high-swirl and no-swirl configurations computed using RANS or LES modeling. The contribution of each uncertain inlet parameter to the variance (in %) is plotted for each combination of flow configuration and turbulence modeling, keeping in mind (Table I) that S_w is fixed to zero for the no-swirl case and that LES modeling makes use of T_i for the no-swirl case only and does not make use of L_t at all. The overwhelming influence of the T_i uncertainty on the RANS high-swirl computations is clearly illustrated (with a contribution equal to 96% of the variance in that case). For the RANS no-swirl case, the uncertainties on both inlet turbulent conditions T_i and L_t contribute to more than 90% of the variance.

The maximum variance associated with the LES computation of the high-swirl flow is explained by both uncertain parameters retained in that case, namely U_b and S_w, with respective contributions of 75% and 24%. Similarly, the maximum variance associated with the LES computation of the no-swirl flow is explained by both uncertain parameters retained in that case, namely U_b and T_i, with respective contributions of 80% and 20%.

5. CONCLUSION

In this paper, numerical simulations of the turbulent flow in a pipe with an axisymmetric expansion have been performed, taking into account uncertain inflow conditions to allow a more realistic comparison with experimental data than when using fully deterministic simulations only. Two different ways of treating turbulence, namely a RANS and a LES approach, have been used. The inherent uncertainties due to the experimental setup under study are the fluctuations around the prescribed

DOI: 10.1002/fld

bulk velocity and swirl number. Moreover, some inlet quantities needed for numerical approach are not controlled or not measured in experiments : they are the inlet turbulence length scale specifically needed for RANS simulations and the inlet turbulence intensity. If no well-established rules exist to determine their values, these quantities have also to be considered as uncertain. In this work, the experimental uncertainties on the computed flow have been analyzed using a non-intrusive polynomial chaos approach as this approach allows to perform the uncertainty quantification process with an acceptable computational cost. Two flow configurations, respectively with and without swirl, have been studied. Comparisons between the expected value and variance of the computed stochastic solutions and the measured value of the experimental data including error measurement provide a solid ground to assess the reliability of the numerical simulations, with respect to a usual purely deterministic approach. For the high-swirl configuration, the RANS simulation is found to be inaccurate to reproduce the experimental mean axial distributions close to the back-flow region generated by the strong swirl. Moreover, the considered inlet uncertainties have a great impact on the numerical prediction in this region. ANOVA analysis shows that the global variance of the RANS computations is essentially due to the uncertainty on the inlet turbulence intensity used to define the inlet condition of the turbulent kinetic energy transport equation. When using LES modeling, the mean solution is globally in good agreement with measured data, and the variance due to uncertain conditions remain within the estimated experimental error bars. For the no-swirl configuration, both RANS and LES approaches lead to a satisfactory agreement with experimental data, and the variance remains systematically small. In this case, ANOVA analysis shows a more balanced contribution of the various uncertain parameters to the global variance. The methodology developed in this work for analyzing turbulent flows in the presence of inlet flow uncertainties for a given configuration is readily applicable to other flows and also to other types of uncertainties such as those existing on the calibration coefficients of the turbulence models. When a LES strategy is considered, the uncertainty quantification methodology can be applied in particular to better understand the influence of the methods in use to prescribe the time-dependent disturbance at the inlet boundary. Future work on the pipe geometry thoroughly investigated in the present study as far as inlet flow uncertainties are concerned will focus on the analysis of modeling or epistemic uncertainties, keeping the distinctive feature of a simultaneous study of RANS and LES approaches.

REFERENCES

1. Lübcke H, Schmidt S, Rung T, Thiele F. Comparison of LES and RANS in bluff-body flows. *Journal of Wind Engineering and Industrial Aerodynamics* 2001; **89**:1471–1485.
2. Breuer M, Jovicic N, Mazaev K. Comparison of DES, RANS and LES for the separated flow around a flat plate at high incidence. *International Journal for Numerical Methods in Fluids* 2003; **41**:357–388.
3. Richez F, Mary I, Gleize V, Basdevant C. Zonal RANS/LES coupling simulation of a transitional and separated flow around an airfoil near stall. *Theoretical and Computational Fluid Dynamics* 2008; **22**:305–315.
4. Boudier G, Gicquel L, Poinsot T, Bissires D, Bérat C. Comparison of LES, RANS and experiments in an aeronautical gas turbine combustion chamber. *Proceedings of the Combustion Institute* 2007; **31**:3075–3082.
5. Santiago J, Dejoan A, Martilli A, Martin F, Pinelli A. Comparison between LES and RANS computations for the must field experiment. *Boundary Layer Meteorology* 2010; **135**:109–132.
6. Tominaga Y, Stathopoulos T. CFD modeling of pollution dispersion in a street canyon: comparison between LES and RANS. *Journal of Wind Engineering and Industrial Aerodynamics* 2011; **99**:340–348.
7. Xie Z, Castro I. LES and RANS for turbulent flow over arrays of wall-mounted obstacles. *Flow Turbulence and Combustion* 2006; **76**:291–312.
8. Constantinescu G, Krajewski W, Ozdemir C, Tokyay T. Simulation of airflow around rain gauges comparison of LES with RANS models. *Advances in Water Resources* 2007; **30**:43–58.
9. Liu Y, Tucker P, Iacono G. Comparison of zonal RANS and LES for a non-isothermal ribbed channel flow. *International Journal of Heat and Fluid Flows* 2006; **27**:391–401.
10. Chang Y, Scotti A. Modeling unsteady turbulent flows over ripples: RANS vs LES. *Journal of Geophysical Research - Oceans* 2004; **109**:C09 012.
11. Rhea S, Bini M, Fairweather M, Jones W. RANS modelling and LES of a single-phase, impinging plane jet. *Computers and Chemical Engineering* 2009; **33**:1344–1353.
12. Cinnella P, Congedo P, Parussini L, Pediroda V. Quantification of thermodynamic uncertainties in real gas flows. *International Journal of Engineering Systems Modelling and Simulation* 2010; **2**:12–24.
13. Najm H, Debusschere B, Marzouk Y, Widmer S, Maitre OL. Uncertainty quantification in chemical systems. *International Journal for Numerical Methods in Engineering* 2009; **80**:789–814.

DOI: 10.1002/fld

14. Le Maitre O, Knio O. *Spectral Methods for Uncertainty Quantification*. Springer: New York, 2010.
15. Lin G, Su CH, Karniadakis G. Predicting shock dynamics in the presence of uncertainties. *Journal of Computational Physics* 2006; **217**:260–276.
16. Lucor D, Meyers J, Sagaut P. Sensitivity analysis of large-eddy simulations to subgrid-scale-model parametric uncertainty using polynomial chaos. *Journal of Fluid Mechanics* 2007; **585**:255–279.
17. Ko J, Lucor D, Sagaut P. Sensitivity of two-dimensional spatially developing mixing layers with respect to uncertain inflow conditions. *Physics of Fluids* 2008; **20**(077102):20.
18. Han X, Sagaut P, Lucor D. On sensitivity of RANS simulations to uncertain turbulent inflow conditions. *Computers & Fluids* 2012; **61**:2–5.
19. Loeven GJA, Bijl H. Airfoil analysis with uncertain geometry using the probabilistic collocation method. *49th AIAA/ASME/ASCE/AHS/ASC Structures, Structural Dynamics, and Materials Conference*, Schaumburg, IL, USA, April 7–10, 2008; 1–11.
20. Platteeuw PDA, Loeven GJA, Bijl H. Uncertainty quantification applied to the k-epsilon model of turbulence using the probabilistic collocation method. *49th AIAA/ASME/ASCE/AHS/ASC Structures, Structural Dynamics, and Materials Conference*, Schaumburg, IL, USA, April 7–10, 2008; 1–17.
21. Dinescu C, Smirnov S, Hirsch C, Lacor C. Assessment of intrusive and non-intrusive non-deterministic CFD methodologies based on polynomial chaos expansions. *International Journal of Engineering Systems Modelling and Simulation* 2010; **2**:87–98.
22. Th Crestaux OLM, Martinez J. Polynomial chaos expansion for sensitivity analysis. *Reliability Engineering & System Safety* 2009; **94**:1161–1172.
23. Congedo PM, Corre C, Martinez JM. Shape optimization of an airfoil in a BZT flow with multiple-source uncertainties. *Computer Methods in Applied Mechanics and Engineering* 2011; **200**(1–4):216–232.
24. Dellenback PA, Metzger DE, Neitzel GP. Measurements in turbulent swirling flow through an abrupt expansion. *AIAA Journal* 1987; **26**(6):669–681.
25. Schlüter JU, Pitsch H, Moin P. Large eddy simulation inflow conditions for coupling with Reynolds-averaged flow solvers. *AIAA Journal* 2004; **42**(3):478–484.
26. Gyllenram W, Nilsson H. Design and validation of a scale-adaptive filtering technique for LRN turbulence modeling of unsteady flow. *Journal of Fluids Engineering* 2008; **130**(2):194–204.
27. Jones WP, Launder BE. The prediction of laminarization with a two-equation model of turbulence. *International Journal of Heat and Mass Transfer* 1972; **15**:301–314.
28. Germano M, Piomelli U, Moin P, Cabot WH. A dynamic subgrid-scale eddy viscosity model. *Physics of Fluids A* 1991; **3**:1760–1765.
29. Issa RI. Solution of implicitly discretized fluid flow equations by operator-splitting. *Journal of Computational Physics* 1986; **62**:40–65.
30. Rhie C, Chow WL. Numerical study of the turbulent flow past an airfoil with trailing edge separation. *AIAA Journal* 1983; **21**:1525–1532.
31. Ferziger JH, Perić M. *Computational methods for fluid dynamics*. Springer: Berlin, New York, 1997.
32. Orlanski I. A simple boundary condition for unbounded hyperbolic flows. *Journal of Computational Physics* 1976; **21**:251–269.
33. Klein A, Sadiki A, Janicka J. A digital filter based generation of inflow data for spatially developing direct numerical or large eddy simulations. *Journal of Computational Physics* 2003; **186**:652–665.
34. Jarrin N, Benhamadouche S, Laurence D, Prosser R. A synthetic-eddy-method for generating inflow conditions for large-eddy simulations. *International Journal of Heat and Fluid Flow* 2006; **27**:585–593.
35. Davidson L. Hybrid LES-RANS: inlet boundary conditions for flows including recirculation. *5th International Symposium on Turbulence and Shear Flow Phenomena*, TU Munich, 2007; 689–694.
36. Xia J, Smith B, Benim A, Schmidli J, Yadigaroglu G. Effect of inlet and outlet boundary conditions on swirling flows. *Computers & Fluids* 1997; **26**:811–823.
37. Yeh CL. Turbulent flow simulation of liquid jet emanating from pressure-swirl atomizer. *Heat Mass Transfer* 2008; **44**:275–280.
38. Cole D, Glauser M. Flying hot-wire measurements in an axisymmetric sudden expansion. *Experimental Thermal and Fluid Science* 1998; **18**:150–167.
39. Ghanem R, Spanos S. *Stochastic Finite Elements: A Spectral Approach*. Springer-Verlag, 1991.
40. Xiu D, Karniadakis G. The Wiener–Askey polynomial chaos for stochastic differential equations. *Journal of Scientific Computing* 2002; **26**:275–280.
41. Cameron R, Martin W. The orthogonal development of nonlinear functionals in series of Fourier–Hermite functionals. *The Annals of Mathematics* 1947; **48**:385–392.
42. Saltelli A, Tarantola S, Campolongo F. *Sensitivity Analysis in Practice*. Wiley: Chichester, 2004.
43. Sobol I. Sensitivity estimates for nonlinear mathematical models. *Mathematical Modeling and Computational Experiment* 1993; **1**:407–414.
44. Orszag SA, Bissonnette LR. Dynamical properties of truncated Wiener–Hermite expansions. *Physics of Fluids* 1967; **10**(12):2603–2613.

DOI: 10.1002/fld